

## EDGE ARTICLE

Cite this: *Chem. Sci.*, 2021, 12, 15308

All publication charges for this article have been paid for by the Royal Society of Chemistry

Plasmonic O<sub>2</sub> dissociation and spillover expedite selective oxidation of primary C–H bonds†Hao Li,<sup>ab</sup> Huan Shang,<sup>c</sup> Fuze Jiang,<sup>ab</sup> Xingzhong Zhu,<sup>id d</sup> Qifeng Ruan,<sup>e</sup> Lizhi Zhang<sup>id c</sup> and Jing Wang<sup>id \*ab</sup>

Manipulating O<sub>2</sub> activation *via* nanosynthetic chemistry is critical in many oxidation reactions central to environmental remediation and chemical synthesis. Based on a carefully designed plasmonic Ru/TiO<sub>2-x</sub> catalyst, we first report a room-temperature O<sub>2</sub> dissociation and spillover mechanism that expedites the “dream reaction” of selective primary C–H bond activation. Under visible light, surface plasmons excited in the negatively charged Ru nanoparticles decay into hot electrons, triggering spontaneous O<sub>2</sub> dissociation to reactive atomic <sup>•</sup>O. Acceptor-like oxygen vacancies confined at the Ru–TiO<sub>2</sub> interface free Ru from oxygen-poisoning by kinetically boosting the spillover of <sup>•</sup>O from Ru to TiO<sub>2</sub>. Evidenced by an exclusive isotopic O-transfer from <sup>18</sup>O<sub>2</sub> to oxygenated products, <sup>•</sup>O displays a synergistic action with native <sup>•</sup>O<sub>2</sub><sup>-</sup> on TiO<sub>2</sub> that oxidizes toluene and related alkyl aromatics to aromatic acids with extremely high selectivity. We believe the intelligent catalyst design for desirable O<sub>2</sub> activation will contribute viable routes for synthesizing industrially important organic compounds.

Received 21st August 2021  
Accepted 26th October 2021

DOI: 10.1039/d1sc04632b

rsc.li/chemical-science

## Introduction

Our Earth's atmosphere is relatively rich in molecular oxygen (O<sub>2</sub>). This is attributed to the photosynthesis by cyanobacteria that led to the “great oxidation event” about 2.5 billion years ago. The high reduction potential of O<sub>2</sub> makes it an excellent green oxidizing agent, while the triplet ground state of O<sub>2</sub>, with two unpaired electrons occupying two antibonding π orbitals in the same spin direction, represents a significant challenge for its robust utilization.<sup>1</sup> To overcome this prominent difficulty, nature evolves families of metalloproteins, which contain unpaired d-electrons, to metabolize O<sub>2</sub> *via* stepwise reduction.<sup>2</sup> In light of this, heterogeneous catalysts with redox transition metal centers were fabricated accordingly to mimic the functionality of enzymatic O<sub>2</sub> utilization.<sup>3,4</sup> The investigation of these processes is known collectively as O<sub>2</sub> activation, aiming at integrating environmentally benign substances into global industrialization that encompasses a critical set of applications,

including fuel cells, environmental remediation, and most importantly, fine chemical synthesis.<sup>5</sup> Unfortunately, compared with metalloproteins, which can be operated under ambient conditions, artificial O<sub>2</sub> activation still suffers from poor efficiency. For instance, the rates of selective (partial) oxidation reactions (ethylene epoxidation, alcohol transformation, and CH<sub>4</sub> oxidation) are kinetically limited by the stubborn O–O double bond of O<sub>2</sub> towards dissociation.<sup>4,6–8</sup> To surmount the energy barrier, high operating temperatures are usually crucial if decent oxidation rates are to be expected. Paradoxically, thermal heating decreases energy efficiencies for numerous inherent exothermic oxidation reactions, compromises the long-term stability of catalysts, or gives rise to low product selectivity.<sup>6,9–11</sup> To this end, developing alternative technologies that enable efficient O<sub>2</sub> activation under ambient temperatures is currently an ambitious goal pursued by worldwide researchers.

Solar light is a clean and limitless energy source that can meet the world's energy needs. From a sustainable chemistry perspective, a conceptually promising approach for facile O<sub>2</sub> activation is heterogeneous photocatalysis.<sup>12–15</sup> By virtue of the photo-excited charge carriers, O<sub>2</sub> can be easily activated to a series of reactive oxygen species (ROS) at room temperature, including <sup>•</sup>O<sub>2</sub><sup>-</sup>, O<sub>2</sub><sup>2-</sup>, <sup>1</sup>O<sub>2</sub>, and <sup>•</sup>OH. However, one serious drawback of photocatalytic O<sub>2</sub> activation is that ROS are usually randomly generated.<sup>13,16</sup> Since different ROS show distinct redox chemistry (interactions) with a specific reactant, multiple thermodynamic reaction pathways, mediated by various co-existing ROS, can proceed simultaneously.<sup>17,18</sup> Thus, without precise tuning of ROS, unwanted toxic intermediates or

<sup>a</sup>Institute of Environmental Engineering, ETH Zürich, Zürich 8093, Switzerland. E-mail: jing.wang@ifu.baug.ethz.ch

<sup>b</sup>Laboratory for Advanced Analytical Technologies, Empa, Swiss Federal Laboratories for Materials Science and Technology, Dübendorf 8600, Switzerland

<sup>c</sup>Laboratory of Pesticide & Chemical Biology of Ministry of Education, Institute of Applied & Environmental Chemistry, College of Chemistry, Central China Normal University, Wuhan 430079, China

<sup>d</sup>College of Science, Nanjing University of Aeronautics and Astronautics, Nanjing 210016, China

<sup>e</sup>Engineering Product Development, Singapore University of Technology and Design, Singapore 487372, Singapore

† Electronic supplementary information (ESI) available. See DOI: 10.1039/d1sc04632b



byproducts will emerge, giving rise to low selectivity for target molecules.<sup>1,19</sup> In this context, manipulating photocatalytic O<sub>2</sub> activation towards the generation of desirable ROS is intuitively valid and theoretically reliable for efficient and selective oxidation reactions. The traditional viewpoint on manipulating photocatalytic O<sub>2</sub> activation is overwhelmingly focused on tuning the electronic structures of photocatalysts. On the surface molecular level, the collaborative development of modern material characterizations and computations, as motivated by nanosynthetic chemistry, highlights that delicate surface structures (exposed surface, native defects, and interfacial configurations) play a more pivotal role in defining the activation manner of small ambient molecules (H<sub>2</sub>O, CO<sub>2</sub>, N<sub>2</sub>).<sup>13,20–22</sup> Therefore, the integration of surface science with photocatalytic O<sub>2</sub> activation opens a new avenue to regulate the generation and transformation of desirable ROS in foreseen scenarios.

Here, we report a new O<sub>2</sub> activation mechanism based on a carefully designed nanostructured Ru/TiO<sub>2–x</sub> photocatalyst. The Ru nanocatalyst on the TiO<sub>2–x</sub> (oxygen-deficient TiO<sub>2</sub> substrate), in the negatively charged state, is highlighted here to trigger room-temperature O<sub>2</sub> dissociation through surface plasmons. The acceptor-like oxygen vacancies confined at the interface kinetically boost <sup>18</sup>O diffusion and spillover from Ru to TiO<sub>2</sub>, thus avoiding oxygen-poisoning and catalyst deactivation. The spillover O<sub>2</sub>, in the form of atomic <sup>18</sup>O, is highly active, and together with native <sup>18</sup>O<sub>2</sub><sup>–</sup> on TiO<sub>2</sub>, it can expedite the “dream reaction” of selective primary C–H bond activation. Evidenced by an exclusive isotopic <sup>18</sup>O-transfer phenomenon, this novel photocatalyst oxidizes toluene into benzoic acid with selectivity over 97% under visible light. Mechanistic insights into the plasmonic O<sub>2</sub> dissociation and spillover scheme, as well as the origination of the high selectivity, are comprehensively discussed on the basis of theoretical and experimental results. As a proof-of-concept, several other related alkyl aromatics are used to showcase the potential of Ru/TiO<sub>2–x</sub> for extended applications.

## Results and discussion

### Theoretical scenarios of O<sub>2</sub> adsorption, activation, and dissociation

TiO<sub>2</sub> is the most widely studied photocatalyst owing to its high abundance and chemical stability. However, O<sub>2</sub> interacts weakly with the perfect TiO<sub>2</sub> surface, impeding photoelectron-driven O<sub>2</sub> activation. Thus, we sought to construct a multifunctional nanostructure to manipulate O<sub>2</sub> activation using TiO<sub>2</sub> as the primary building block.<sup>23</sup> The first ingredient we considered was the oxygen vacancies (OVs), which are the most common anion defects to promote oxygen adsorption and diffusion.<sup>24,25</sup> The second building block we thought of was Ru due to the following two reasons. First, Ru catalyst with d-band electrons shows a very high affinity to O<sub>2</sub>. It has been extensively employed for thermally driven catalytic oxidations, including CO, CH<sub>4</sub>, alcohol, acid, alkene, and biomass oxidations.<sup>26</sup> Second, after being downsized to the nanoscale regime, nano-sized Ru displays strong interactions with the oscillating

electric field of the incident light, known as the localized surface plasmon resonance (LSPR) phenomenon.<sup>27–30</sup> LSPR excitation is accompanied by the generation of abundant plasmons or hot electrons that may be energetic enough to activate O<sub>2</sub> at room temperature. Density functional theory (DFT) calculation was then performed to depict the O<sub>2</sub> adsorption, activation, and possible dissociation processes on Ru/TiO<sub>2</sub> nanocomposites. Anatase(101) is one of the representative surfaces of TiO<sub>2</sub> with high thermodynamic stability. We optimized the geometric structure of the anatase(101) surface with an OV on the O row (TiO<sub>2–x</sub>). A 10-atom Ru (Ru<sub>10</sub>) cluster with a hexagonal close-packed crystal structure, which usually represents nanoparticles, was placed on the bridging O row close to the OV on TiO<sub>2–x</sub> to construct a Ru/TiO<sub>2–x</sub> composite structure (Fig. 1a). According to the charge density difference, the Ru<sub>10</sub> cluster became negatively charged (Fig. 1a). Bader charge analysis demonstrated that the electron-rich OV center at the interface transferred (donated) one of its localized electrons to Ru<sub>10</sub>. Those negatively charged Ru atoms close to the interfacial OV with low steric hindrance were deemed extremely active for O<sub>2</sub> adsorption and activation. As expected, the O<sub>2</sub> adsorption on negatively charged Ru<sub>10</sub> was exergonic by 3.76 eV (Fig. 1b). Consistent with the enormous adsorption energy, the O–O bond of O<sub>2</sub> was largely activated to 1.43 Å, close to that of O<sub>2</sub><sup>2–</sup> (1.48 Å). Based on the spin of adsorbed O<sub>2</sub> that was composed of an occupied majority and minority state without any magnetic moment, the activated O<sub>2</sub> on Ru/TiO<sub>2–x</sub> was reconfirmed to be O<sub>2</sub><sup>2–</sup> species (Fig. 1c).<sup>31</sup> In contrast, for the Ru<sub>10</sub> cluster on defect-free TiO<sub>2</sub> (Ru/TiO<sub>2</sub>), O<sub>2</sub> adsorption was only exergonic by 2.45 eV with a slightly stretched O–O bond length of 1.32 Å (Fig. 1b). Clearly, with an OV confined at the Ru–TiO<sub>2–x</sub> interface, both O<sub>2</sub> adsorption and activation on Ru<sub>10</sub> were remarkably strengthened. After identifying the O<sub>2</sub> pre-activation state, we were curious about whether O<sub>2</sub> dissociation would proceed further. For O<sub>2</sub> on the ground state potential energy surface (PES), its dissociation is encountered by an intense energy barrier ascribed to the strong O–O double bond, suggesting that room-temperature O<sub>2</sub> dissociation is energy demanding (Fig. 1d). Interestingly, with an OV at the Ru–TiO<sub>2–x</sub> interface, O<sub>2</sub> dissociation became thermodynamically favorable with a negligible energy barrier of +0.10 eV (Fig. 1b). For O<sub>2</sub> on Ru/TiO<sub>2</sub> in a much weaker activation state, its dissociation, by comparison, was strongly endergonic by +2.58 eV.

Following O<sub>2</sub> dissociation, the next step we considered was the transportation of the dissociated O<sub>2</sub>. The ideal case is that part of the <sup>18</sup>O can be transferred to the TiO<sub>2</sub> surface so that Ru is free from O<sub>2</sub> poisoning and readily “pumps” <sup>18</sup>O to the TiO<sub>2</sub> surface, where reactant adsorption takes place. Such a step can be denoted as O<sub>2</sub> spillover, a general concept in thermocatalysis that depicts the migration of reactive species adsorbed on one surface to another surface that does not adsorb or generate the species directly under the same conditions.<sup>32</sup> According to the transition state (TS), even though <sup>18</sup>O spillover from Ru<sub>10</sub> to TiO<sub>2</sub> was exergonic by 1.62 eV, the kinetic barrier was as large as +0.89 eV (Fig. 1b). Interestingly, <sup>18</sup>O could easily spillover to the OV confined at the Ru/TiO<sub>2–x</sub> atomic interface with an energy release of 3.88 eV. Moreover, the kinetic barrier of <sup>18</sup>O spillover

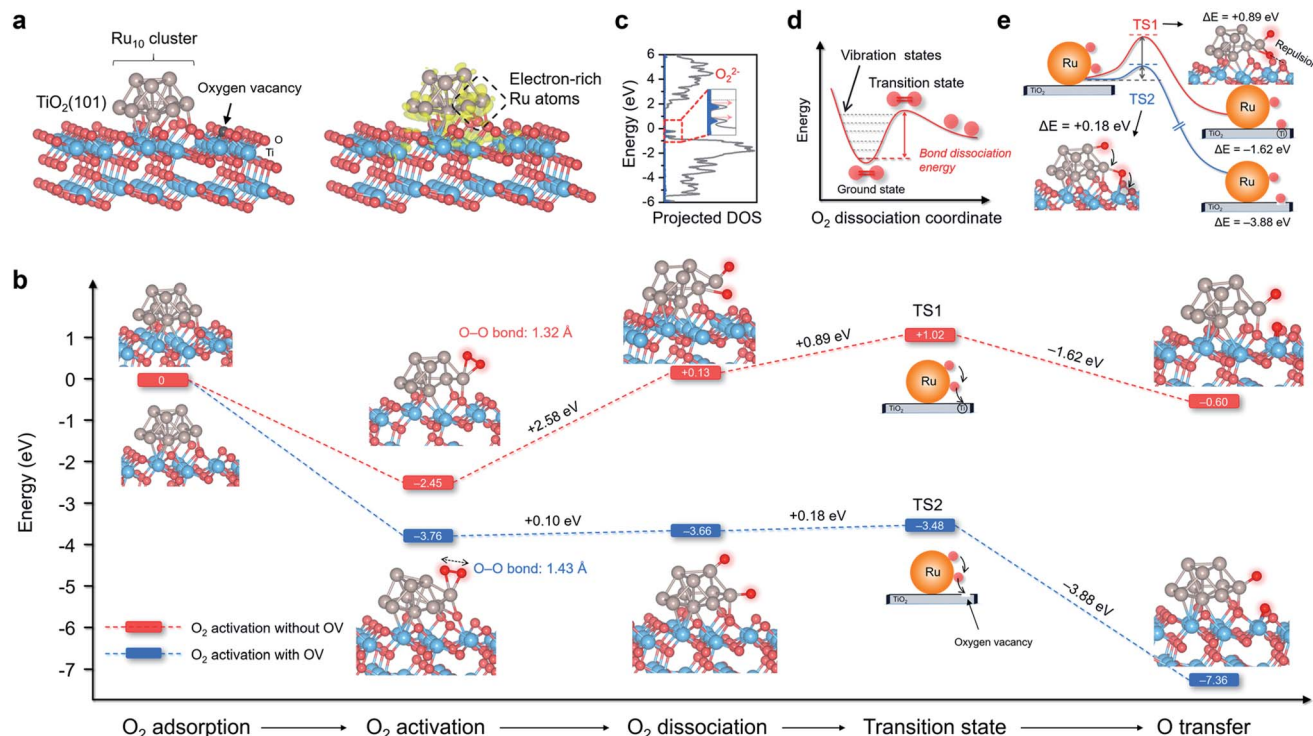


**Fig. 1** Thermodynamics and kinetics of O<sub>2</sub> activation, dissociation, and spillover on Ru<sub>10</sub> cluster/anatase(101) surface with and without OV. (a) The theoretical model of Ru/TiO<sub>2-x</sub>. The charge density localization on the Ru<sub>10</sub> cluster is shown on the right side. The yellow isosurface with an isovalue of 0.005 au represents spatial charge accumulation. (b) Free energy change against the reaction coordinates for O<sub>2</sub> activation, dissociation, and spillover over Ru/TiO<sub>2</sub> with and without OV. (c) Molecular density of states projected on highly activated O<sub>2</sub> adsorbed on Ru/TiO<sub>2-x</sub>. For clarity, the spin-down plots are not shown here. (d) Schematic illustration of the potential energy surface towards O<sub>2</sub> dissociation. (e) Transition states associated with O atom spillover from Ru<sub>10</sub> to TiO<sub>2</sub> substrate with and without OV.

towards the OV was remarkably reduced to +0.18 eV (Fig. 1b). After a careful examination of the sophisticated TS structures, we found that 'O spillover on Ru/TiO<sub>2</sub> was restricted by the interfacial steric hindrance and the sizeable electrostatic repulsion with lattice O (Fig. 1e). In contrast, the OV confined at the Ru-TiO<sub>2-x</sub> interface acted as a perfect oxygen acceptor and readily accommodated the spillover 'O, which well explained the thermodynamic and kinetic feasibility of oxygen spillover (Fig. 1e).

### Synthesis of the Ru/TiO<sub>2-x</sub> photocatalyst

Enlightened by the theoretical results, both O<sub>2</sub> dissociation and spillover on Ru/TiO<sub>2-x</sub> were envisioned as highly practicable through acceptor-like OV under mild conditions. To verify our hypothesis, a Ru/TiO<sub>2-x</sub> nanocomposite was prepared accordingly. The preparation process was associated with the preliminary reduction of commercial TiO<sub>2</sub> by NaBH<sub>4</sub> through calcination to obtain TiO<sub>2</sub> with abundant surface OVs (TiO<sub>2-x</sub>). Then, Ru<sub>3</sub>(CO)<sub>12</sub>, impregnated on TiO<sub>2-x</sub>, was reduced by a gaseous mixture of H<sub>2</sub> and Ar (1 : 9, v/v) at 350 °C to obtain Ru/TiO<sub>2-x</sub> (Fig. 2a). For comparison, we synthesized Ru/TiO<sub>2</sub> through the same H<sub>2</sub>-annealing method only by replacing TiO<sub>2-x</sub> with defect-free TiO<sub>2</sub>. Transmission electron microscopy (TEM) showed that Ru/TiO<sub>2-x</sub> consisted of nanoparticles with diameters ranging from 20 to 60 nm

(Fig. 2b). Ru nanoparticles with an average size of 2 nm were highly dispersed on TiO<sub>2-x</sub>, which appeared brighter on the high-angular annular dark field-scanning transmission electron microscopy (HAADF-STEM) image due to the heavier atomic mass of Ru than that of Ti (Fig. 2c and d). Corresponding energy dispersive X-ray (EDX) mapping images showed that the support was composed of Ti and O, while the bright spots were made of Ru (Fig. 2d). The high-resolution TEM (HRTEM) image demonstrated the crystalline nature of native TiO<sub>2-x</sub> and loaded Ru nanoparticles (Fig. 2e). The clear lattice fringes with a spacing of 0.35 nm and 0.21 nm corresponded to the anatase(101) and hexagonal Ru(101) atomic planes, respectively.

### Characterizations of the plasmonic Ru/TiO<sub>2-x</sub> photocatalyst

X-ray diffraction (XRD) patterns revealed that the introduction of OVs and Ru nanoparticles did not change the crystal structure of TiO<sub>2</sub>, consistent with the TEM images (Fig. S1a†). No diffraction peaks assigned to Ru nanoparticles were detected in the XRD patterns of Ru/TiO<sub>2</sub> or Ru/TiO<sub>2-x</sub>, possibly because the surface Ru content (~2 atom%) was below the detection limit. The Ru K-edge X-ray absorption near-edge structure (XANES) spectra of Ru/TiO<sub>2-x</sub> were significantly away from RuO<sub>2</sub>, but were slightly shifted to lower energies compared to that of Ru foil, indicating that the metallic Ru nanoparticles on TiO<sub>2-x</sub>



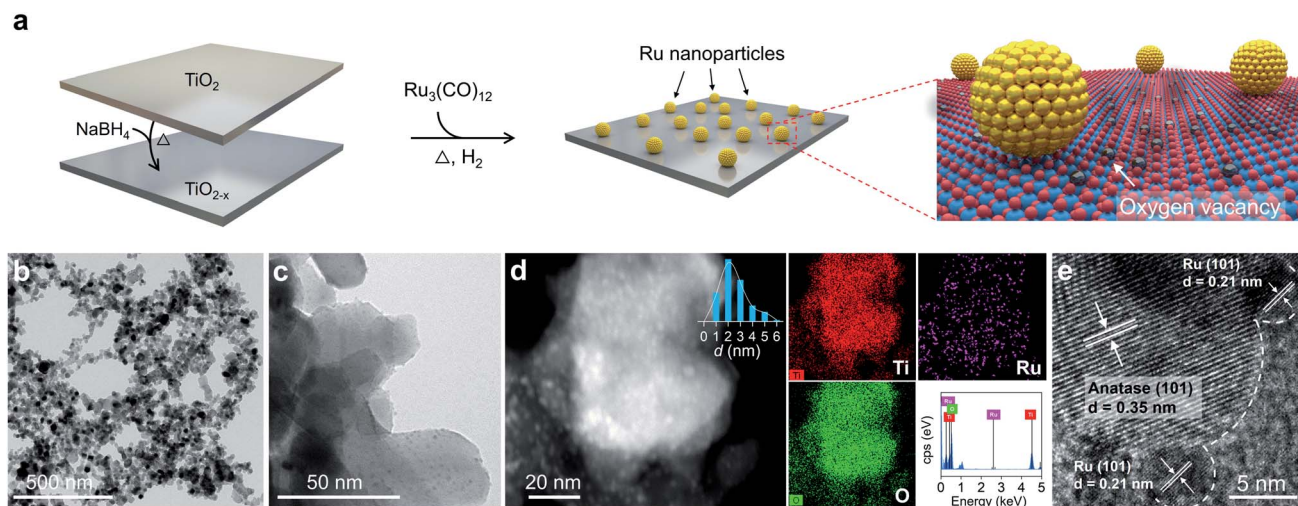


Fig. 2 Preparation and electron microscopy characterization of the Ru/TiO<sub>2-x</sub> photocatalyst. (a) Schematic illustration of the Ru/TiO<sub>2-x</sub> preparation process. (b and c) TEM images of Ru/TiO<sub>2-x</sub>. (d) HAADF-STEM and EDX mapping images of Ru/TiO<sub>2-x</sub>. (e) HRTEM image of Ru/TiO<sub>2-x</sub>.

were negatively charged (Fig. 3a). We further adopted X-ray absorption fine structure (XAFS) to investigate the Ru atom relaxation behaviors. The Fourier transform of Ru K-edge extended XAFS oscillation curves of Ru/TiO<sub>2</sub> and Ru/TiO<sub>2-x</sub> were close to Ru foil but different from that of RuO<sub>2</sub>, reconfirming the metallic nature of the Ru nanoparticles (Fig. 3b).

Interestingly, the Ru–Ru bond of Ru/TiO<sub>2-x</sub> (~2.5 Å) was notably longer than that of Ru/TiO<sub>2</sub> or Ru foil (~2.3 Å) based on the XAFS oscillation curves, suggesting the electrostatic repulsion within a negatively charged Ru nanoparticle (Fig. 3b). Consistent with the theoretical calculation, the OV of TiO<sub>2-x</sub> could donate part of their localized electrons, thus negatively

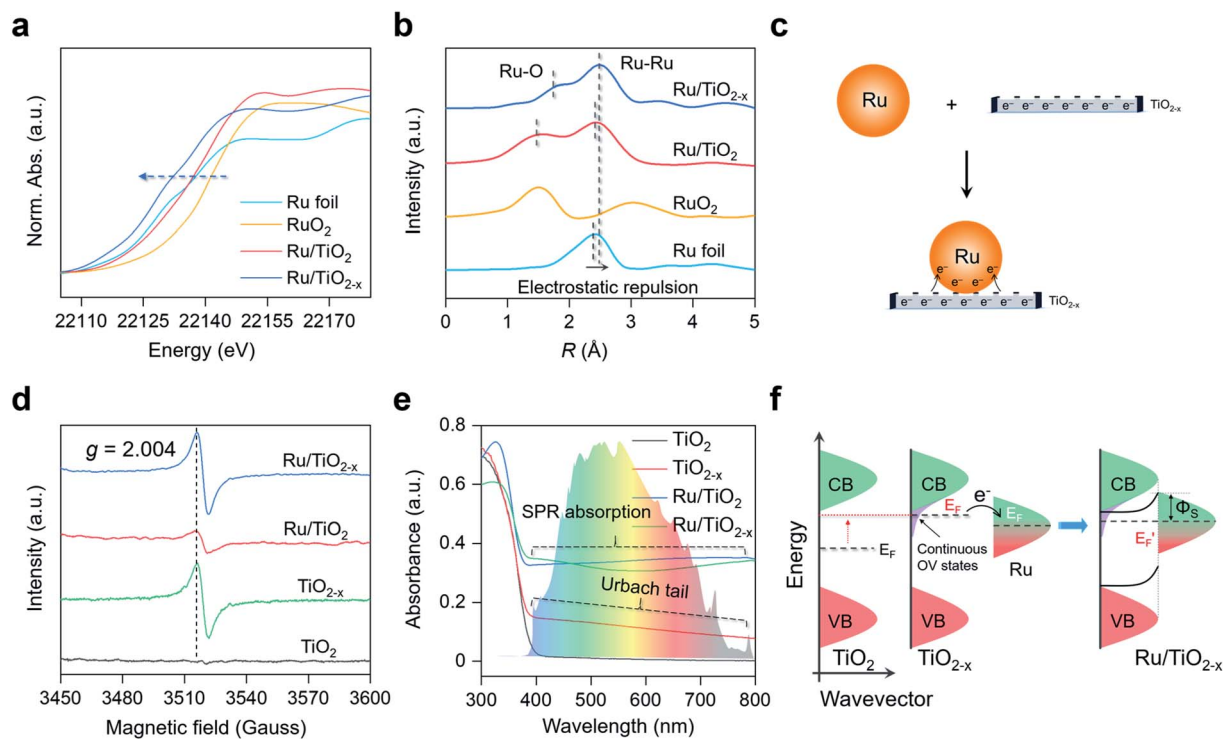


Fig. 3 Characterization of the as-prepared TiO<sub>2</sub>, TiO<sub>2-x</sub>, Ru/TiO<sub>2</sub>, and Ru/TiO<sub>2-x</sub>. (a) XANES spectra, (b) Fourier transforms of Ru K-edge extended XAFS oscillations of the as-prepared photocatalysts. (c) Schematic illustration of the negatively charged Ru on TiO<sub>2-x</sub>. (d) EPR and (e) UV-vis absorption spectra of the as-prepared photocatalysts. (f) Schematic illustration of the interfacial charge transfer and Schottky barrier formation at the Ru–TiO<sub>2-x</sub> interface.

charging the neighboring Ru nanoparticle and causing electrostatic repulsions (Fig. 3c).

Electron paramagnetic resonance (EPR) is a versatile technique to probe the type and concentration of defects. According to room-temperature EPR,  $\text{TiO}_{2-x}$  and  $\text{Ru/TiO}_{2-x}$  possessed a symmetrical and comparable signal with the specific  $g$  factor at 2.004 that corresponded to OV $^{\cdot}$ s (Fig. 3d). The OV $^{\cdot}$ s were also reflected by the two additional shoulder peaks with lower binding energies at 463.2 eV and 458.0 eV in the Ti 2p high-resolution X-ray photoelectron spectroscopy (XPS), assigned to the  $\text{Ti}^{3+}$  species around the OV $^{\cdot}$ s (Fig. S1b $\dagger$ ). The concentration of OV $^{\cdot}$ s on  $\text{TiO}_{2-x}$  was quantitatively determined by the percentage of  $\text{Ti}^{3+}$  species, which was estimated to be 37% based on XPS analysis (Fig. S1b $\dagger$ ). A weak OV signal appeared on  $\text{Ru/TiO}_2$  due to the  $\text{H}_2$ -annealing process that slightly reduced the  $\text{TiO}_2$  substrate (Fig. 3d). Compared to white  $\text{TiO}_2$  with an absorption edge around 400 nm (bandgap  $\sim 3.10$  eV), grayish  $\text{TiO}_{2-x}$  displayed a decaying absorption tail throughout the visible light region, referred to as the Urbach tail (Fig. 3e). The formation of the Urbach tail was induced by the OV-associated electronic states beneath the conduction band (CB) edge.<sup>33–35</sup> With a high concentration of OV $^{\cdot}$ s on the  $\text{TiO}_2$  surface, abundant localized states progressively became hybridized with the CB, giving rise to an exponentially decreased electronic state embedded within the bandgap of  $\text{TiO}_2$  (Fig. 3f). The continuous OV-induced states, which were usually 0–1.5 eV below the CB of  $\text{TiO}_2$ , largely shifted the Fermi level ( $E_F$ ) above that of Ru.<sup>36,37</sup> The upshifted Fermi level enabled localized electron transfer from the OV $^{\cdot}$ s to Ru nanoparticles *via* the interfacial Ru–O bonds until their Fermi levels were aligned at equilibrium, rationalizing the negatively charged Ru nanoparticles on  $\text{TiO}_{2-x}$  (Fig. 3c and S2 $\dagger$ ). Meanwhile, once the thermal equilibrium was reached, a Schottky barrier ( $\Phi_s$ ) was established at the Ru– $\text{TiO}_{2-x}$  interface. As evidenced by steady-state and time-resolved photoluminescence (PL) spectroscopy, both the OV $^{\cdot}$ s and Schottky barrier ( $\Phi_s$ ) contributed to the rapid separation of charge carriers (Fig. S3 and Table S1 $\dagger$ ).<sup>38,39</sup> The finite-difference time-domain (FDTD) simulations reveal that a Ru sphere (diameter of 2 nm) on  $\text{TiO}_2$  displays a plasmonic absorption ranging from 100 nm to 600 nm centered at 215 nm (Fig. S4 $\dagger$ ). The LSPR response of Ru on the  $\text{TiO}_{2-x}$  surface was a pronounced and extended absorption throughout the visible light spectrum (Fig. 3e). Unlike colloidal Au or Ag nanoparticles with representative plasmon resonant absorption peaks, the wide and flat absorption curve of  $\text{Ru/TiO}_{2-x}$  was probably due to the plasmon hybridization effect among nanoparticles in close proximity on defective substrates.<sup>40</sup>

### Study of $\text{O}_2$ dissociation and spillover

After understanding the geometric and electronic structures of  $\text{Ru/TiO}_{2-x}$ , we tried to detect the key ROSs formed at room temperature. According to theoretical calculation, the native ROS on the OV of anatase(101) surface was  $\text{O}_2^{\cdot-}$  (Fig. S5 $\dagger$ ). As evidenced by EPR, upon exposure to visible light, both  $\text{TiO}_{2-x}$  and  $\text{Ru/TiO}_{2-x}$  generated a four-line spectrum with relative intensities of 1 : 1 : 1 : 1 with 5,5-dimethyl-1-pyrroline-*N*-oxide as the spin-trapping reagent, a characteristic signal of  $\text{O}_2^{\cdot-}$  (Fig. 4a).

The same signal was silent over  $\text{Ru/TiO}_2$ , highlighting the pivotal role of OV $^{\cdot}$ s in enabling selective  $\text{O}_2^{\cdot-}$  formation (Fig. 4a). We did not detect any  $\text{OH}^{\cdot}$  signals due to the absence of water in acetonitrile (Fig. S6 $\dagger$ ). The direct detection of atomic  $\text{O}^{\cdot}$  in photocatalytic systems had been scarcely reported. We then sought to detect  $\text{O}_3^{\cdot-}$  species, because if  $\text{O}^{\cdot}$  was spillover to  $\text{TiO}_{2-x}$ , it would probably interact with abundant native  $\text{O}_2^{\cdot-}$  to produce  $\text{O}_3^{\cdot-}$  ( $\text{O}^{\cdot} + \text{O}_2^{\cdot-} \rightarrow \text{O}_3^{\cdot-}$ ).  $\text{O}_3^{\cdot-}$  is described as the combination of  $\text{O}^{\cdot}$  and  $\text{O}_2^{\cdot-}$  through weak covalent bonding, which can be stabilized under low temperature and detected by EPR.<sup>41–43</sup> In the air, irradiated  $\text{Ru/TiO}_{2-x}$  displayed three key parameters at  $g_1 = 2.007$ ,  $g_2 = 2.002$ , and  $g_3 = 1.995$  at 77 K, a hyperfine structure corresponding to  $\text{O}_3^{\cdot-}$  ions (Fig. 4b). Under the same conditions, neither  $\text{TiO}_2$  nor  $\text{TiO}_{2-x}$  afforded  $\text{O}_3^{\cdot-}$  generation, suggesting that  $\text{O}_2$  dissociation was primarily initiated by plasmonic Ru nanoparticles. Meanwhile, the  $\text{O}_3^{\cdot-}$ -EPR spectra of  $\text{Ru/TiO}_{2-x}$  displayed two times stronger peak intensity than  $\text{Ru/TiO}_2$  (Fig. 4b). To directly validate plasmonic  $\text{O}_2$  spillover at room temperature, we performed  $\text{O}_2$ -temperature-programmed desorption ( $\text{O}_2$ -TPD) for the as-prepared photocatalysts after 30 min of visible light irradiation in the air. The  $\text{O}_2$ -TPD profiles showed four types of oxygen species. The peaks at 100–250 °C, 250–400 °C, 400–550 °C, and 550–700 °C can be assigned to surface  $\text{O}_2^{\cdot-}$ , atomic  $\text{O}^{\cdot}$ , lattice O on the surface, and lattice O in the bulk, respectively (Fig. 4c and S7 $\dagger$ ).<sup>43</sup> In agreement with the low-temperature EPR,  $\text{TiO}_2$  and  $\text{TiO}_{2-x}$  showed negligible surface  $\text{O}^{\cdot}$ . However,  $\text{O}_2$ -TPD of  $\text{Ru/TiO}_{2-x}$  exhibited a broad and intense desorption feature from 250 to 400 °C, indicating that spillover  $\text{O}^{\cdot}$  from Ru was enriched on  $\text{TiO}_{2-x}$  (Fig. 4c). Based on the integrated  $\text{O}_2$ -TPD peak area, the concentration of  $\text{O}^{\cdot}$  on  $\text{Ru/TiO}_{2-x}$  was 6 times that of  $\text{Ru/TiO}_2$ , demonstrating that the  $\text{O}_2$  dissociation and spillover on Ru were kinetically promoted by OV $^{\cdot}$ s confined at the Ru– $\text{TiO}_{2-x}$  interface (Fig. S7 and Table S2 $\dagger$ ).

Another direct evidence of room-temperature  $\text{O}_2$  dissociation and spillover was based on the TPD-mass spectrum (TPD-MS) (Fig. 4d). We deposited the Ru nanoparticles onto a  $\text{SiO}_2$  substrate ( $\text{Ru/SiO}_2$ ) for comparison (Fig. S8 $\dagger$ ). With He as the inert feeding gas, none of the photocatalysts exhibited  $\text{O}$ -desorption peaks after visible light irradiation (Fig. 4d). Interestingly, when  $^{18}\text{O}_2$  was used as the feeding oxygen,  $\text{Ru/TiO}_{2-x}$  showed a prominent peak at 335 °C with a mass fraction equal to  $^{18}\text{O}$  (Fig. 4d). The same  $^{18}\text{O}$ -desorption peak on  $\text{Ru/TiO}_2$  was at 328 °C, but much weaker. For  $\text{TiO}_{2-x}$  without Ru deposition, no mass signals of  $^{18}\text{O}$  were witnessed. In the dark,  $\text{O}_2$  dissociation was remarkably suppressed on  $\text{Ru/TiO}_{2-x}$  (Fig. S9 $\dagger$ ). Meanwhile, there was a linear relationship between the relative amount of dissociated  $^{18}\text{O}_2$  and light intensity, serving as the key signature of electron-mediated  $\text{O}_2$  dissociation (Fig. 4e).<sup>6,44</sup> Both transient surface photovoltage and photocurrent response evidenced the enhanced formation of hot electrons on Ru nanoparticles when coupled with  $\text{TiO}_{2-x}$  (Fig. S10 $\dagger$ ). Contingent on the increased thermodynamic feasibility and boosted reaction kinetics, we reasoned that room-temperature  $\text{O}_2$  dissociation on  $\text{Ru/TiO}_{2-x}$  was primarily driven by plasmonic hot electrons. From the kinetic perspective, when surface plasmons of Ru are introduced as the external stimulus, hot electrons can transiently populate the antibonding orbital of  $\text{O}_2$  through

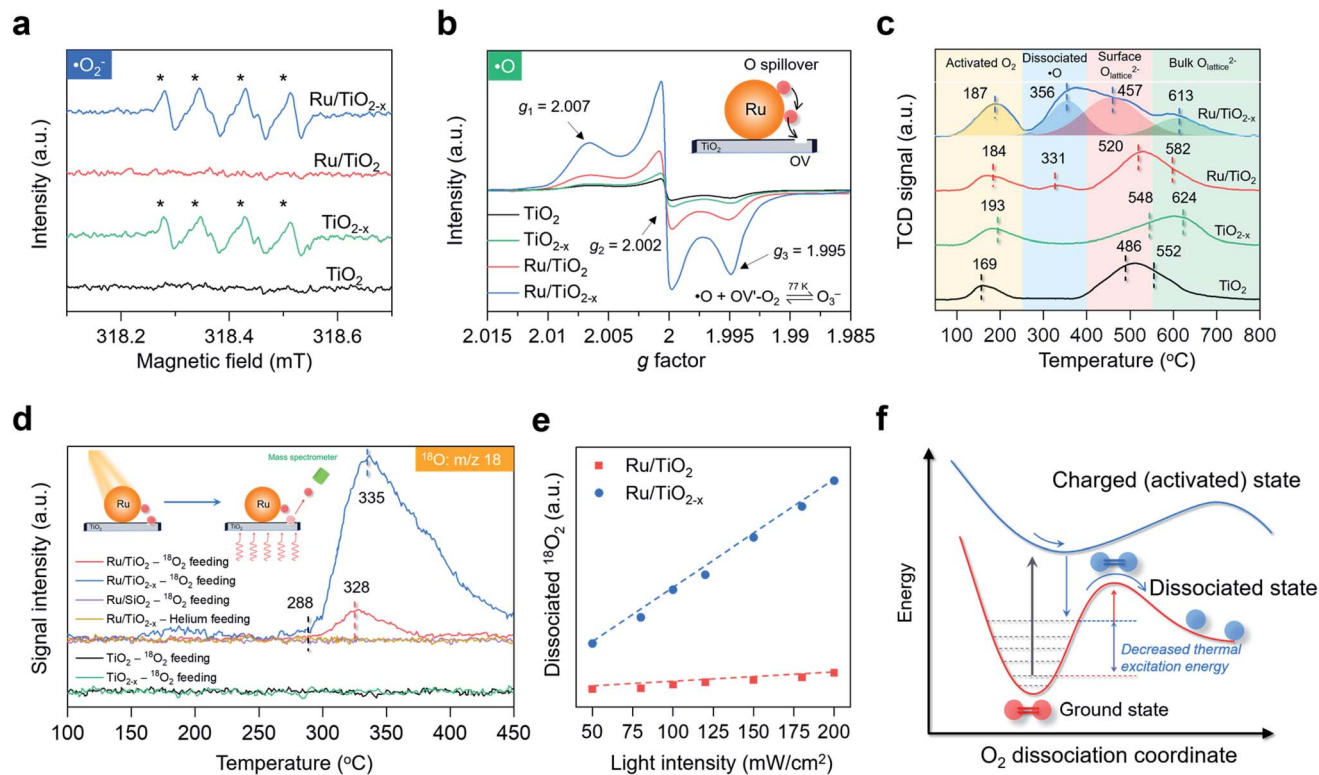


Fig. 4 Investigation of O<sub>2</sub> dissociation and spillover over the as-prepared photocatalysts. (a) Room-temperature EPR spectra of <sup>•</sup>O<sub>2</sub><sup>-</sup> in acetonitrile under visible light. (b) Low-temperature EPR spectra of O<sub>3</sub><sup>-</sup> under visible light. (c) O<sub>2</sub>-TPD spectra of the as-prepared photocatalysts. TCD represents the thermal conductivity detector. (d) O<sup>18</sup> mass signals of the as-prepared photocatalysts after visible light irradiation. Inset represents a schematic illustration of O detection via TPD-MS. (e) The relative amount of dissociated <sup>18</sup>O<sub>2</sub> as a function of the light intensity. Dissociated <sup>18</sup>O<sub>2</sub> was calculated from the desorbed <sup>18</sup>O-TPD-MS peak area. The dashed lines show the linear fit between temperature and dissociated <sup>18</sup>O<sub>2</sub>. (f) Schematic illustration of plasmonic hot electron-driven O<sub>2</sub> dissociation. The curves show the potential energy surface towards O<sub>2</sub> dissociation.

plasmon decay and electron scattering that are highly dependent on the metal–O<sub>2</sub> interplay.<sup>29,30</sup> Thanks to the strong interactions between O<sub>2</sub> and negatively charged Ru on TiO<sub>2-x</sub>, the dynamic plasmonic hot electron transfer from excited Ru to the antibonding  $\pi$  orbital of O<sub>2</sub> will be kinetically boosted that quickly stretches the O–O bond of O<sub>2</sub> to O<sub>2</sub><sup>2-</sup> species (O<sub>2</sub> + 2e<sup>-</sup> +  $h\nu$  → O<sub>2</sub><sup>2-</sup>). In response to the antibonding orbital population, the nuclear motion along the O–O bond is promoted on the excited PES; still, the movement may not be so drastic to trigger direct O<sub>2</sub> dissociation (overcome the O<sub>2</sub> dissociation barrier) on excited-state PES due to the short lifetime of plasmonic electrons (Fig. 4f). Thus, an appreciable amount of plasmonic electrons decay back to the Ru, reverting O<sub>2</sub><sup>2-</sup> on the excited state PES to the ground state PES. During this decaying process, the plasmonic energy is not released but instead stored (deposited) in the O–O chemical bond (O<sub>2</sub><sup>2-</sup> – 2e<sup>-</sup> → O<sub>2</sub><sup>\*</sup>), keeping O<sub>2</sub> at a relatively high vibrational state with a much lowered thermal excitation energy barrier towards dynamic dissociation (Fig. 4f).<sup>29,30,45</sup>

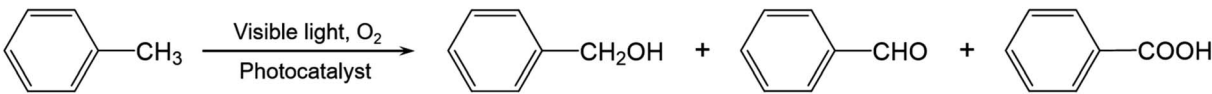
### Selective primary C–H bond activation and mechanism

Activation of primary C–H bonds has long been the “dream reaction” to produce high-value-added chemicals from

inexpensive raw chemicals. Unfortunately, traditional strategies with transition metal-complexes as the catalysts necessitate hazardous and refractory oxygen donors to drive the selective activation of the inert C(sp<sup>3</sup>)-H bonds under harsh conditions (*e.g.*, high pressure and high temperature with strong acidic or basic additives).<sup>46–49</sup> Inspired by the novel plasmonic O<sub>2</sub> dissociation and spillover phenomenon, we systematically evaluated the photoreactivity and selectivity of Ru/TiO<sub>2-x</sub> for C–H bond activation at room temperature (26 °C). Using toluene, the simplest member of alkyl aromatics, as the model substrate, we found that TiO<sub>2</sub>, TiO<sub>2-x</sub>, and Ru/TiO<sub>2</sub> could successfully activate the primary C–H bonds of toluene under visible light. However, the conversion efficiencies remained low and the oxygenated product was a mixture of benzyl alcohol, benzaldehyde, and benzoic acid (Table 1). Subsequent separation and purification of the desired product add to the complexity of this process. Remarkably, Ru/TiO<sub>2-x</sub> showed the highest toluene conversion efficiency (95.1%) with an impressive 97.1% selectivity towards benzoic acid (Table 1). Temporal evolution of intermediates and products showed that benzaldehyde and benzoic acid had been the dominant products of TiO<sub>2-x</sub> (Fig. 5a). For Ru/TiO<sub>2-x</sub>, benzaldehyde and benzoic acid accounted for large fractions of oxidized toluene in the first 2 hours, whereafter benzoic acid gradually predominated (Fig. 5a). This provided direct evidence



Table 1 Photocatalytic oxidation of toluene by the as-prepared photocatalysts under visible light at room temperature (26 °C)<sup>a</sup>

					
Photocatalyst	Conversion (%)	Product selectivity (%)			
		Benzyl alcohol	Benzaldehyde	Benzoic acid	CO <sub>2</sub>
TiO <sub>2</sub>	18.8	9.7	50.3	38.2	1.8
TiO <sub>2-x</sub>	46.2	5.8	78.4	14.6	1.2
Ru/TiO <sub>2</sub>	26.3	3.8	29.1	65.6	1.5
Ru/TiO <sub>2-x</sub>	95.1	0.6	1.2	97.1	1.1
Ru/SiO <sub>2</sub>	18.4	10.8	47.8	39.8	1.6

<sup>a</sup> Reactions were carried out in 5 mL CH<sub>3</sub>CN solution, containing 0.1 mmol toluene and 50 mg photocatalyst at an O<sub>2</sub> balloon pressure under a 300 W Xe lamp with a 400 nm cutoff filter. Acetonitrile was used as the solvent instead of water to avoid <sup>•</sup>OH generation. The distributions and concentrations of the products were determined by gas chromatography-mass spectrometry (GC-MS) at different reaction times.

that toluene was oxidized to benzoic acid by Ru/TiO<sub>2-x</sub> in a sequential manner. After another 4 cycles of photocatalytic toluene oxidation, Ru/TiO<sub>2-x</sub> maintained its selectivity and reactivity (Fig. 5b). The XRD pattern, HRTEM image, and EPR spectra indicated that Ru/TiO<sub>2-x</sub> was catalytically stable after multicycle photocatalytic toluene oxidation even though the concentration of OVs was slightly decreased (Fig. S11<sup>†</sup>). By comparison, Ru/SiO<sub>2</sub> obtained a low toluene oxidation efficiency, consistent with the limited O<sub>2</sub> dissociation capability on Ru/SiO<sub>2</sub> (Table 1 and Fig. 4d). For a physical mixture of Ru nanoparticles and TiO<sub>2-x</sub>, its toluene oxidation was 52.5%, much lower than that of Ru/TiO<sub>2-x</sub>, highlighting the delicate Ru–TiO<sub>2-x</sub> interactions in promoting photocatalytic toluene oxidation (Table S3<sup>†</sup>). It should be mentioned that the temperature of the solvent gradually increased from 25 to 41 °C

without a cooling system with Ru/TiO<sub>2-x</sub> as the photocatalyst under visible light. To rule out the contribution of increased temperature, we carried out toluene oxidation subject to a water bath heating that kept the temperature at 41 °C. Ru/TiO<sub>2-x</sub> only obtained a 10.1% conversion efficiency in the dark at 41 °C (Table S3<sup>†</sup>). Increasing the sizes of Ru nanoparticles on TiO<sub>2-x</sub> led to decreased efficiency for selective photocatalytic toluene oxidation, possibly due to occupied OVs, inhibited reactant adsorption, and decreased interfacial area (Fig. S12<sup>†</sup>).

To clarify the high selectivity of toluene oxidation towards benzoic acid, we focused on the contribution of different ROSs. When the reaction atmosphere was switched from O<sub>2</sub> to Ar, the photo-conversion efficiency of Ru/TiO<sub>2-x</sub> decreased dramatically to 13.9%, revealing that the primary oxidant was O<sub>2</sub> (Fig. S13<sup>†</sup>). Then, different scavengers of reactive species were

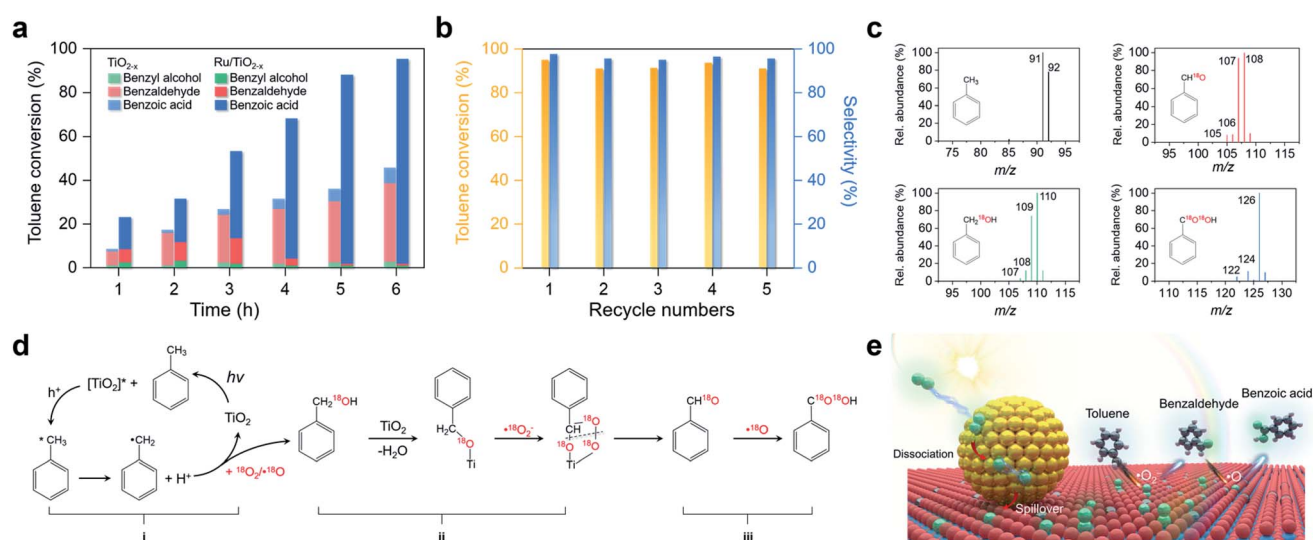


Fig. 5 Selective photocatalytic oxidation of toluene and the proposed mechanism. (a) The temporal toluene conversion efficiency and selectivity over Ru/TiO<sub>2-x</sub> and TiO<sub>2-x</sub>. (b) Multicycle selective toluene oxidation by Ru/TiO<sub>2-x</sub>. (c) Mass spectra of the oxygenated products with <sup>18</sup>O<sub>2</sub> as the oxidant generated by Ru/TiO<sub>2-x</sub> after 3 hours of photoreaction. (d) Proposed mechanism for selective photocatalytic toluene oxidation to benzoic acid. (e) Schematic illustration of the plasmonic dissociation and spillover for selective toluene oxidation.

introduced into the reaction system. After  $\text{AgNO}_3$  was added to trap electrons, toluene conversion over  $\text{TiO}_{2-x}$  and  $\text{Ru/TiO}_{2-x}$  decreased significantly (Fig. S13†). As  $\text{O}_2$  alone could not oxidize toluene at room temperature, the electron-mediated  $\text{O}_2$  activation was considered vital for toluene oxidation. The addition of sodium oxalate ( $\text{Na}_2\text{C}_2\text{O}_4$ ) as the hole scavenger also suppressed toluene oxidation of  $\text{TiO}_{2-x}$  and  $\text{Ru/TiO}_{2-x}$  (Fig. S13†). The addition of benzoquinone as the  $\cdot\text{O}_2^-$  scavenger completely terminated toluene oxidation by  $\text{TiO}_{2-x}$ . However, benzoquinone partially suppressed toluene oxidation by  $\text{Ru/TiO}_{2-x}$  accompanied by a decreased selectivity towards benzoic acid (Fig. S13 and Table S4†). This result suggested that besides  $\cdot\text{O}_2^-$ , the contribution of another important ROS, presumably the  $\cdot\text{O}$ , was indispensable to achieve a high benzoic acid selectivity. When tetra-methylpiperidine *N*-oxide (TEMPO) was added as a net scavenger for radical oxygen species ( $\cdot\text{O}_2^- + \cdot\text{O}$ ), oxidation of toluene by  $\text{Ru/TiO}_{2-x}$  was inhibited entirely (Fig. S13†). Clearly, the spillover  $\cdot\text{O}$  worked together with native  $\cdot\text{O}_2^-$  on  $\text{TiO}_{2-x}$  to expedite primary C–H bond activation of toluene for selective benzoic acid synthesis.

To unveil the selective toluene oxidation mechanism, we carried out  $^{18}\text{O}_2$  isotopic labeling experiments. After 2 hours of photoreaction, about 92% of benzyl alcohol and benzaldehyde molecules generated by  $\text{Ru/TiO}_{2-x}$  were  $^{18}\text{O}$ -labeled, ruling out the contribution of lattice O from  $\text{TiO}_2$  for toluene oxidation *via* the Mars–van Krevelen mechanism (Fig. 5c). After 6 hours of photoreaction, over 84% of the benzoic acid contained two  $^{18}\text{O}$  atoms (Fig. 5c). Meanwhile, the kinetic isotope effect (KIE) of  $\text{O}_2$  was 1.28 and 1.72 for  $\text{TiO}_{2-x}$  and  $\text{Ru/TiO}_{2-x}$ , respectively (Fig. S14†). The KIE difference indicated that plasmonic  $\text{O}_2$  dissociation and spillover on  $\text{Ru/TiO}_{2-x}$  was more kinetically relevant to toluene oxidation than  $\text{TiO}_{2-x}$ . Based on the results and discussion, we drew a plausible pathway for selective toluene oxidation by  $\text{Ru/TiO}_{2-x}$  (Fig. 5d). The first critical step was the activation of the primary C–H bonds in toluene by photoholes to form benzyl radical (i in Fig. 5d). The benzyl radical (carbon-centered radical) was evidenced by EPR with *n*-tertbutyl- $\alpha$ -phenylnitron (PBN) as the spin-trapping reagent (Fig. S15†). Benzyl radicals then reacted with  $^{18}\text{O}_2$  or  $\cdot^{18}\text{O}$  to yield the  $^{18}\text{O}$ -labelled benzyl alcohol *via* an O-insertion reaction. Due to the selective production of  $\cdot\text{O}_2^-$  on native  $\text{TiO}_{2-x}$ , benzyl alcohol was further oxidized to benzaldehyde through an O-exchange reaction between  $\cdot\text{O}_2^-$  and  $\alpha$ -carbon of benzyl alcohol *via* an oxygen-bridged structure (ii in Fig. 5d).<sup>17</sup> This step was verified by using  $^{16}\text{O}$ -benzyl alcohol as the substrate and  $^{18}\text{O}_2$  as the oxidant, which showed that  $^{18}\text{O}$ -labelled benzaldehyde emerged as the primary product on  $\text{Ru/TiO}_{2-x}$  (Fig. S16†). By increasing the concentration of OVs in  $\text{Ru/TiO}_{2-x}$ , both photocatalytic toluene oxidation efficiency and selectivity were gradually increased (Fig. S17†). Since the Ru nanoparticles on Ru readily “pumped”  $\cdot\text{O}$  onto the  $\text{TiO}_{2-x}$  surface through spillover, the major ROS responsible for the further oxidation of benzaldehyde into benzoic acid should be  $\cdot^{18}\text{O}$  (iii in Fig. 5d and e). This final step was further evidenced using  $^{16}\text{O}$ -benzaldehyde and  $^{18}\text{O}_2$  as the oxidant.  $\text{TiO}_{2-x}$  showed poor photoreactivity for benzaldehyde oxidation, while  $\text{Ru/TiO}_{2-x}$  selectively produced benzoic acid as the final product

that contained one  $^{18}\text{O}$  atom (Fig. S18†). Overall, the selective activation of the primary C–H bonds in toluene resulted from the synergistic interaction between spillover  $\cdot\text{O}$  and native  $\cdot\text{O}_2^-$  (Fig. 5e).  $\text{Ru/TiO}_{2-x}$  was also active and selective for the oxidation of primary C–H bonds of a wide variety of substituted toluenes (Table S5†).

## Conclusions

In conclusion, guided by nanosynthetic chemistry, we first reported a room-temperature  $\text{O}_2$  dissociation and spillover mechanism that expedited the “dream reaction” of selective primary C–H bond activation with a plasmonic  $\text{Ru/TiO}_{2-x}$  catalyst. Under visible light, surface plasmons excited in negatively charged Ru nanoparticles decayed into hot electrons, triggering spontaneous  $\text{O}_2$  dissociation to reactive atomic  $\cdot\text{O}$ . Acceptor-like oxygen vacancies confined at the Ru– $\text{TiO}_2$  interface freed Ru from oxygen-poisoning by kinetically boosting the spillover of  $\cdot\text{O}$  from Ru to  $\text{TiO}_2$ . Evidenced by an exclusive isotopic O-transfer from  $^{18}\text{O}_2$  to oxygenated products,  $\cdot\text{O}$  displayed a synergistic action with native  $\cdot\text{O}_2^-$  on  $\text{TiO}_2$  that oxidized toluene into benzoic acid with selectivity over 97%. The  $\text{Ru/TiO}_{2-x}$  was also active and selective for a number of other related alkyl aromatics with great potential for extended applications. We believe the intelligent photocatalyst design for desirable  $\text{O}_2$  activation will contribute viable routes for synthesizing industrially important organic compounds.

## Methods

### Catalyst preparation

To prepare  $\text{TiO}_{2-x}$ , we thoroughly mixed 2 g commercial Degussa P25  $\text{TiO}_2$  with 1 g  $\text{NaBH}_4$ . The mixture was then transferred to a porcelain crucible with a cap and annealed at 300 °C (temperature increase rate: 10 °C  $\text{min}^{-1}$ ) in the air using a muffle furnace for 20 min. After naturally cooling down to room temperature, the grayish  $\text{TiO}_{2-x}$  was repeatedly washed with deionized water and ethanol 6 times to remove unreacted  $\text{NaBH}_4$ , followed by vacuum drying at 80 °C. To prepare  $\text{Ru/TiO}_{2-x}$ , 1 g of  $\text{TiO}_{2-x}$  was dispersed in tetrahydrofuran that contained  $\text{Ru}_3(\text{CO})_{12}$ . The atomic percentage ratio of Ru to Ti was adjusted to 2 atom%. After 4 hours of impregnation in an Ar atmosphere, the black suspension was directly vacuum dried at 50 °C. Then, the black powder was reduced by a gaseous mixture of  $\text{H}_2$  and Ar (1 : 9, v/v) at 350 °C for 1 hour to obtain  $\text{Ru/TiO}_{2-x}$ . For comparison,  $\text{Ru/TiO}_2$  and  $\text{Ru/SiO}_2$  were prepared through the same method only by replacing  $\text{TiO}_{2-x}$  with Degussa P25 and commercial  $\text{SiO}_2$ .

### Photocatalytic toluene oxidation

In a typical process, photocatalytic toluene oxidation was carried out in 5 mL  $\text{CH}_3\text{CN}$  that contained 0.1 mmol toluene. 50 mg photocatalyst was thoroughly immersed in the toluene solution and transferred to a 10 mL quartz tube. The  $\text{CH}_3\text{CN}$  was first bubbled with  $\text{O}_2$  for 30 min to remove other dissolved gases completely. Then, the quartz tube was sealed with



a balloon that was prefilled with O<sub>2</sub> of high purity. Subsequently, the mixture was magnetically stirred for 1 hour in the dark in order to reach adsorption–desorption equilibrium. A water bath system was used to maintain the temperature of the quartz tube at around 26 °C. After light irradiation by a 300 W xenon lamp (Perfectlight: PLS-SXE 300) with a 400 nm cutoff filter for a certain time, the suspension was centrifuged and filtered with a nylon syringe filter (0.22 μm) to completely remove the nanoparticles. The oxygenated products in the solution were analyzed and determined with a gas chromatography-mass spectrometry instrument (Agilent Technologies, GC6890N, MS 5973, capillary column: HP-5MS, 30 m × 0.25 mm, 0.25 μm). The conversion efficiency of toluene and the selectivity for certain oxygenated products are defined as conversion (%) =  $[(C_i - C_T)/C_i] \times 100\%$  and selectivity (%) =  $[C_O/(C_i - C_T)] \times 100\%$ , where C<sub>i</sub> is the initial concentration of toluene, C<sub>T</sub> and C<sub>O</sub> are respectively the concentrations of the detected toluene and corresponding oxygenated product. Typical <sup>18</sup>O<sub>2</sub>-labeling photocatalytic experiments were carried out under the same conditions by replacing the O<sub>2</sub> atmosphere with <sup>18</sup>O<sub>2</sub> (97 atom% <sup>18</sup>O).

## Data availability

All experimental and theoretical supporting data are provided in the ESI.†

## Author contributions

H. L. and J. W. supervised the project. H. L. designed and carried out the experiments. H. S. and H. L. carried out the DFT calculations. X. Z. Z. and Q. F. R. carried out the FDTD simulation. F. Z. J. and L. Z. Z. contributed to the data analysis. H. L. and J. W. wrote the paper. All the authors discussed results and provided comments during the manuscript preparation.

## Conflicts of interest

There are no conflicts to declare.

## Acknowledgements

This work was supported by ETH Zürich Foundation and Center for Filtration Research (CFR) at the University of Minnesota.

## Notes and references

- 1 E. Romero, J. R. Gómez Castellanos, G. Gadda, M. W. Fraaije and A. Mattevi, *Chem. Rev.*, 2018, **118**, 1742–1769.
- 2 A. Decker and E. I. Solomon, *Curr. Opin. Chem. Biol.*, 2005, **9**, 152–163.
- 3 V. L. Sushkevich, D. Palagin, M. Ranocchiari and J. A. van Bokhoven, *Science*, 2017, **356**, 523–527.
- 4 E. Tabor, J. Dedecek, K. Mlekodaj, Z. Sobalik, P. C. Andrikopoulos and S. Sklenak, *Sci. Adv.*, 2020, **6**, eaaz9776.
- 5 M. M. Montemore, M. A. van Spronsen, R. J. Madix and C. M. Friend, *Chem. Rev.*, 2018, **118**, 2816–2862.
- 6 P. Christopher, H. Xin and S. Linic, *Nat. Chem.*, 2011, **3**, 467–472.
- 7 I. X. Green, W. Tang, M. Neurock and J. T. Yates, *Science*, 2011, **333**, 736–739.
- 8 A. Wittstock, V. Zielasek, J. Biener, C. M. Friend and M. Baumer, *Science*, 2010, **327**, 319–322.
- 9 J. Lu, J. Bravo-Suárez, A. Takahashi, M. Haruta and S. Oyama, *J. Catal.*, 2005, **232**, 85–95.
- 10 S. Linic, U. Aslam, C. Boerigter and M. Morabito, *Nat. Mater.*, 2015, **14**, 567–576.
- 11 C. T. Campbell, *Science*, 2002, **298**, 811–814.
- 12 B. Yang, Y. Chen and J. Shi, *Chem. Rev.*, 2019, **119**, 4881–4985.
- 13 H. Li, Z. Ai and L. Zhang, *Chem. Commun.*, 2020, **56**, 15282–15296.
- 14 C. Clavero, *Nat. Photonics*, 2014, **8**, 95–103.
- 15 R. Jiang, B. Li, C. Fang and J. Wang, *Adv. Mater.*, 2014, **26**, 5274–5309.
- 16 Y. Nosaka and A. Y. Nosaka, *Chem. Rev.*, 2017, **117**, 11302–11336.
- 17 M. Zhang, Q. Wang, C. Chen, L. Zang, W. Ma and J. Zhao, *Angew. Chem., Int. Ed.*, 2009, **48**, 6081–6084.
- 18 C. Mao, H. Cheng, H. Tian, H. Li, W.-J. Xiao, H. Xu, J. Zhao and L. Zhang, *Appl. Catal., B*, 2018, **228**, 87–96.
- 19 B. G. Malmstrom, *Annu. Rev. Biochem.*, 1982, **51**, 21–59.
- 20 Y.-F. Li, U. Aschauer, J. Chen and A. Selloni, *Acc. Chem. Res.*, 2014, **47**, 3361–3368.
- 21 K. Zhao, L. Zhang, J. Wang, Q. Li, W. He and J. J. Yin, *J. Am. Chem. Soc.*, 2013, **135**, 15750–15753.
- 22 N. G. Petrik and G. A. Kimmel, *J. Phys. Chem. Lett.*, 2011, **2**, 2790–2796.
- 23 S. A. Rawool, K. K. Yadav and V. Polshettiwar, *Chem. Sci.*, 2021, **12**, 4267–4299.
- 24 A. Tilocca and A. Selloni, *ChemPhysChem*, 2005, **6**, 1911–1916.
- 25 R. Schaub, *Science*, 2003, **299**, 377–379.
- 26 M. R. Axet and K. Philippot, *Chem. Rev.*, 2020, **120**, 1085–1145.
- 27 J. M. Sanz, D. Ortiz, R. Alcaraz de la Osa, J. M. Saiz, F. González, A. S. Brown, M. Losurdo, H. O. Everitt and F. Moreno, *J. Phys. Chem. C*, 2013, **117**, 19606–19615.
- 28 X. Meng, T. Wang, L. Liu, S. Ouyang, P. Li, H. Hu, T. Kako, H. Iwai, A. Tanaka and J. Ye, *Angew. Chem., Int. Ed.*, 2014, **53**, 11478–11482.
- 29 P. Christopher, H. Xin and S. Linic, *Nat. Chem.*, 2011, **3**, 467–472.
- 30 S. Linic, P. Christopher and D. B. Ingram, *Nat. Mater.*, 2011, **10**, 911–921.
- 31 H. Li, H. Shang, Y. Li, X. Cao, Z. Yang, Z. Ai and L. Zhang, *Environ. Sci. Technol.*, 2019, **53**, 6964–6971.
- 32 W. C. Conner and J. L. Falconer, *Chem. Rev.*, 1995, **95**, 759–788.
- 33 H. Yaghoubi, Z. Li, Y. Chen, H. T. Ngo, V. R. Bhethanabotla, B. Joseph, S. Ma, R. Schlaf and A. Takshi, *ACS Catal.*, 2015, **5**, 327–335.

- 34 J. Swaminathan and S. Ravichandran, *J. Phys. Chem. C*, 2018, **122**, 1670–1680.
- 35 B. Choudhury and A. Choudhury, *Phys. E*, 2014, **56**, 364–371.
- 36 H. Tan, Z. Zhao, M. Niu, C. Mao, D. Cao, D. Cheng, P. Feng and Z. Sun, *Nanoscale*, 2014, **6**, 10216–10223.
- 37 C. Mao, L. Yu, J. Li, J. Zhao and L. Zhang, *Appl. Catal., B*, 2018, **224**, 612–620.
- 38 S. Luo, X. Ren, H. Lin, H. Song and J. Ye, *Chem. Sci.*, 2021, **12**, 5701–5719.
- 39 Z. Fan, X. Huang, C. Tan and H. Zhang, *Chem. Sci.*, 2015, **6**, 95–111.
- 40 L. Zhou, Y. Tan, J. Wang, W. Xu, Y. Yuan, W. Cai, S. Zhu and J. Zhu, *Nat. Photonics*, 2016, **10**, 393–398.
- 41 M. Che and A. J. Tench, *Adv. Catal.*, 1983, 1–148.
- 42 V. V. Nikisha, B. N. Shelimov, V. A. Shvets, A. P. Griva and V. B. Kazansky, *J. Catal.*, 1973, **28**, 230–235.
- 43 J. Yang, S. Hu, Y. Fang, S. Hoang, L. Li, W. Yang, Z. Liang, J. Wu, J. Hu, W. Xiao, C. Pan, Z. Luo, J. Ding, L. Zhang and Y. Guo, *ACS Catal.*, 2019, **9**, 9751–9763.
- 44 P. Christopher, H. Xin, A. Marimuthu and S. Linic, *Nat. Mater.*, 2012, **11**, 1044–1050.
- 45 S. Linic, P. Christopher, H. Xin and A. Marimuthu, *Acc. Chem. Res.*, 2013, **46**, 1890–1899.
- 46 L. Kesavan, R. Tiruvalam, M. H. A. Rahim, M. I. bin Saiman, D. I. Enache, R. L. Jenkins, N. Dimitratos, J. A. Lopez-Sanchez, S. H. Taylor, D. W. Knight, C. J. Kiely and G. J. Hutchings, *Science*, 2011, **331**, 195–199.
- 47 W. Partenheimer, *Catal. Today*, 1995, **23**, 69–158.
- 48 A. K. Suresh, M. M. Sharma and T. Sridhar, *Ind. Eng. Chem. Res.*, 2000, **39**, 3958–3997.
- 49 T. W. Bastock, J. H. Clark, K. Martin and B. W. Trenbith, *Green Chem.*, 2002, **4**, 615–617.